Materials Chemistry and Physics 311 (2024) 128525

Contents lists available at ScienceDirect

Materials Chemistry and Physics

journal homepage: www.elsevier.com/locate/matchemphys

High porosity-magnetic composite materials for magnetic induction swing adsorption (MISA): Improvement of performance properties

Mariangela Bellusci [a], Martin Albino [b,c], Andrea Masi [d], Davide Peddis [e], Claudia Innocenti [b], Francesca Varsano [a,*]

[a] ENEA C.R. Casaccia, Via Anguillarese 301, 00123, Roma, Italy
[b] Dept. of Chemistry and INSTM U. Schiff, Univ. of Florence, via della Lastruccia 3, 50019, Sesto Fiorentino, FI, Italy
[c] ICCOM – CNR, via Madonna del Piano 10, 50019, Sesto Fiorentino, FI, Italy
[d] ENEA C.R. Frascati, Via E. Fermi 45, Frascati, RM, Italy
[e] Dipartimento di Chimica e Chimica Industriale e INSTM Università degli Studi di Genova, Via Dodecaneso 31, Genova, 1–16146, Italy

HIGHLIGHTS

- MISA can contribute to the electrification of chemical processes.
- Fe_3O_4@HKUST-1 composite is synthesized and characterized.
- Fe_3O_4@HKUST-1 acts as a smart sorbent for CO_2/N_2 separation.
- Design of the nanoparticles dimension is needed to maximize the composite heating power.
- Induction heating is superior to the conventional heating in terms of desorption rates.

GRAPHICAL ABSTRACT

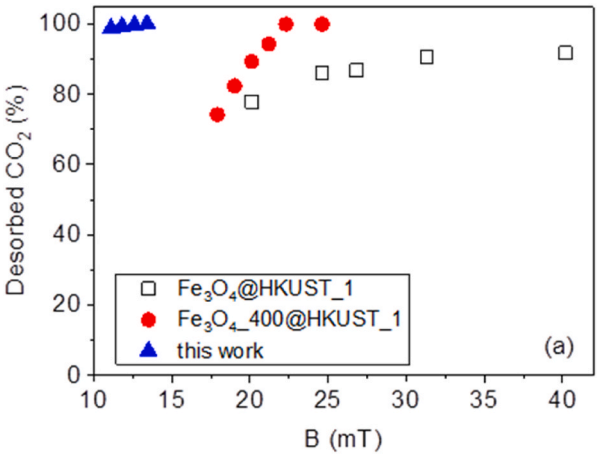

ARTICLE INFO

Keywords:
Induction heating
Electrification
Magnetic composites
HKUST-1
CO_2/N_2 separation
CO_2 adsorption

ABSTRACT

A magnetic composite consisting of MOF HKUST-1 and magnetite nanoparticles was synthesized and successfully utilized for the separation of CO_2 from N_2/CO_2 mixtures. The CO_2 adsorbed by the porous material was successively desorbed by means of a recently proposed, high-efficiency technique so-called Magnetic Induction Swing Adsorption (MISA). The energy necessary to the desorption of carbon dioxide is transferred by electromagnetic induction to the magnetic nanoparticles that promptly dissipate it into heat. The composite material has been synthesized by growing the metal organic framework on functionalized magnetite nanoparticles by means of liquid assisted grinding (LAG) mechanochemical process. The composite material has been characterized in its morphological and functional properties. Thanks to improved magnetic properties, the optimized nanocomposite requires lower magnetic fields to desorb the CO_2 and allows for reaching the same regeneration

* Corresponding author.
E-mail address: francesca.varsano@enea.it (F. Varsano).

https://doi.org/10.1016/j.matchemphys.2023.128525
Received 6 July 2023; Received in revised form 13 September 2023; Accepted 5 October 2023
Available online 10 October 2023

temperature in the sorbent bed at lower magnetic field amplitude, compared to previously synthesized composite materials. A regeneration energy Q of 4.4 MJ/kg CO_2 has been calculated at 130 °C desorption temperature.

1. Introduction

Decarbonization of the chemical industry through electrification is a currently proposed solution for reducing anthropogenic greenhouse gas (GHG) emissions. The utilization of electricity to drive chemical conversion processes, as well as separation and purification operations, can be performed through its direct use in electrochemical synthesis of chemicals or through conversion of electrical energy to heat (power-to-heat). In particular, electricity can provide the heat to power endothermic chemical reactions through the use of various electromagnetic sources [1], e.g., induction [2–7], microwave [8–10], plasma [11] or by direct joule heating [12–14].

Magnetic **I**nduction **S**wing **A**dsorption (MISA) is a recently proposed technology [15] with the aim of improving the energy efficiency of gas separation processes, with a particular focus on the regeneration step of adsorbent materials through Temperature Swing Adsorption (TSA). MISA is based on the use of composite materials consisting of a component with high adsorption capacity of the molecules to be separated (in this paper a Metal Organic Framework, MOF) and magnetic nanoparticles that heat up locally under the action of an alternating magnetic field, allowing a rapid and complete regeneration of the sorbent. The electromagnetic energy is converted into thermal energy inside the adsorbent bed, overcoming all resistance to heat transmission. This causes a high regeneration rate of the solid sorbent beds ensuing a greater productivity, when compared with conventional heating systems. Furthermore, localized heating avoids energy waste due to thermal gradients between the walls of the reactor column and the heart of the sorbent bed typical of reactors heated from outside, prefiguring energy savings. When this technology was suggested for the first time, the materials proposed and investigated were mainly Magnetic Framework Composites (MFCs) [16–22]. More recently, the separation technology based on magnetic induction has attracted the strong research interest of several research groups who have experimented it also with composite materials based on traditional adsorbents such as activated carbon and zeolites [23–26]. The electrification of the separation processes is in fact at the center of renewed interest as a method of intensification of energy intensive desorption processes [19]. In a previous paper we reported the development of MFC materials based on HKUST-1 and magnetite nanoparticles for the capture of carbon dioxide from post combustion processes [27]. The HKUST MOF had been chosen for its good CO_2/N_2 selectivity despite moderate working capacity and instability in wet condition that however can be improved with linkers or post-synthesis modification [28]. The composite was synthesized by growing the MOF on the surface of Fe_3O_4 nanoparticles functionalized with trimesic acid (TMA). The developed composites showed a complete release of the adsorbed CO_2 upon the application of a suitable magnetic field, faster than that determined by traditional heating (TSA). Both magnetite nanoparticles and the subsequent growth of HKUST-1 has been synthetized by a mechanochemical process [29].

However, although the liquid assisted grinding synthetic route allows for easily and sustainably obtaining magnetic nanoparticles, it does not allow a fine control on their size and morphology. In fact, what is usually obtained are aggregates of nanoparticles with a fairly wide size distribution. In the previous work the nanoparticles obtained at the end of the synthesis process show size around 5–7 nm, a value which rises up to 15–50 nm after a mild heat treatment, inducing also strong decrease of surface measured by BET [27]. Considering the magnetic relaxation [30,31] as the main mechanism for heat dissipation it should be underlined that particle size distribution and particle aggregation (i.e., increase of interparticle interactions) represent two key factors for hyperthermic efficiency of nanoparticles. In fact due to the exponential dependence of the relaxation time on the nanoparticle volume, just particles with specific volume will contribute efficiently the heat dissipation [32–34]. Despite this topic is still quite controversial in literature [35–38], interparticle interactions can also significantly affect hyperthermic efficiency of the materials, strongly modifying relaxation time and then changing the nanoparticle volume necessary to optimize heat dissipation.

Starting from this landscape [32,33], a new Fe_3O_4@HKUST-1 MFC has been synthetized based on magnetite nanoparticles with controlled morphology (i.e., particles size and shape [39,40]) and limited aggregation (i.e., negligible interparticle interactions), specifically optimized for their application in MISA. Indeed, the final efficiency of the process will depend on how efficiently the nanoparticles dissipate the electromagnetic field.

This paper focuses on the synthesis of such magnetic composite and its structural, morphological and magnetic characterization, discussing its potential in the carbon dioxide/nitrogen separation process. Regeneration efficiency is calculated based on experimentally determined parameters such as carbon dioxide desorption energy, regeneration productivity, and magnetic energy dissipated by the composite.

2. Materials and methods

2.1. Nanoparticles synthesis

The magnetic nanoparticles (MNP) were synthesized by thermal decomposition of iron acetylacetonate ($Fe(acac)_3$), in high-boiling solvent (benzyl ether) in the presence of surfactants (oleic acid, OA and oleylamine, OAM). Since the as-synthesized MNP had a hydrophobic OA surface coating, it was necessary to modify the surface with TMA to facilitate their embedding into HKUST-1.

Synthesis of Fe_3O_4. $Fe(acac)_3$ (2.83 g, 8 mmol), OAM (6.42 g, 24 mmol), OA (6.8 g, 24 mmol) and benzyl ether (60 mL) were mixed and magnetically stirred under a flow of nitrogen in a 250 mL three-neck round-bottom flask for 15 min. The resulting mixture was heated to reflux (~290 °C) at 15 °C/min and kept at this temperature for 90 min under a blanket of nitrogen and vigorous stirring. The black-brown mixture was cooled at room temperature and ethanol (60 mL) was added causing the precipitation of a black powder. The product was magnetically separated with a permanent magnet, washed several times with ethanol and finally re-dispersed in toluene.

Phase transfer by ligand-exchange with TMA. 500 mg of Fe_3O_4 MNP were dispersed in $CHCl_3$ (90 ml), added to a solution of TMA (600 mg) in dimethyl sulfoxide (DMSO,18 ml), sonicated for 1 h and finally incubated at room temperature for 12 h in a rotating agitator. The precipitate was magnetically separated with a permanent magnet, washed several times first with DMSO, then with ethanol and finally dried under N_2 flux.

2.2. Composite synthesis

The synthesis methodology used for the preparation of the composite powders is analogous to that described in our previous work [27]. Briefly, a LAG (liquid assisted grinding) mechanochemical method was applied in two consecutive grinding phases: (i) milling of the TMA coated magnetite NP (0,25 g) in the presence of trimesic acid (0.730 g) and methanol (0.5 ml, 10 min) to favor a good dispersion of Fe_3O_4 nanoparticles in the reactive mixture; (ii) addition of copper acetate (1 g) and of 4.5 ml of methanol to carry out the synthesis of HKUST-1 and making the composite (30 min milling). Both grindings were carried out under Ar atmosphere with 6 zirconia balls (10 mm) in a SPEX 8000 M

mixer/mill. The nanoparticles functionalization step (i) is used to direct the growth of the MOF crystalline structure right on the surface of the magnetite particles, incorporating them. The final product was left to air dry overnight, and purified the next day according to the method set up for the MOF HKUST [27]. The composite density evaluated on the basis of its composition is equal to 1.17 g/cm^3.

2.3. Instrumental characterization

Thermal characterization for verification of the stability range of the material and for the determination of the loading of nanoparticles was performed with a Pyris PerkinElmer Diamond thermobalance in air flow (100 ml/min).

The nitrogen adsorption isotherms at 77 K were performed using a high-resolution Quantachrome Autorsorb iQ instrument. On the basis of the experimental data, the specific surface area was determined by applying the BET method and the porosity distribution by the Quantachrome NovaWin software, simulating the adsorption curve using the Non-Local Density Functional Theory (NLDFT) and applying a calculation model for carbonaceous structures with slit pores [41]. Equilibrium adsorption measurements of nitrogen and carbon dioxide at different temperatures were performed using the Quantachrome Nova2000 instrument on a sample amount of about 200 mg. The working temperature of the sample was controlled by immersing the sample in a circulating water bath (273 K, 298 K, 308 K) or in a heating bag equipped with temperature control (403 K).

The morphology and the average particle sizes of the MNP and nanocomposite were evaluated by transmission electron microscopy (TEM) using a CM12 PHILIPS transmission electron microscope. X-ray powder diffraction (XRD) measurement on MNPs was carried out using a Bruker D8 Advance diffractometer equipped with a Cu Kα radiation (λ = 1.54178 Å) and operating in θ-θ Bragg Brentano geometry at 40 kV and 40 mA. Lattice parameter, *a*, and the mean crystallite diameter, d_{XRD}, were evaluated using the TOPAS® software (Bruker) using the Fundamental Parameter Approach considering a cubic space group Fd-3m. XRD analysis of the nanocomposite was performed using a diffractometer equipped with a 120° linear simultaneous detector from INEL and a monochromatized Fe $K\alpha_1$ source (λ = 1.936 Å).

The surfactant percentage was determined by elemental analysis on carbon, hydrogen, and nitrogen (CHN analysis) by a CHN–S FlashE1112 Thermofinnigan Elementary Analyzer. Elemental analysis was performed by Inductive Coupled Plasma - Atomic Emission Spectroscopy (ICP-AES) by using a Varian 720-ES spectrometer.

Magnetic measurements were performed using a SQUID magnetometer (Quantum Design MPMS) operating in the 2–350 K temperature range with applied fields up to 5 T. The powder samples were hosted in a Teflon tape and then pressed in a pellet to prevent preferential orientation of the crystallites under the magnetic field. The obtained values of magnetization were normalized by the weight of ferrite present in the sample and expressed in Am^2/kg of ferrite. The error on magnetization values is estimated as 2%.

In a typical breakthrough experiment, performed utilizing a Micromeritics Autochem II 2920, the gas mixture is flowed through powder granules (~0,5 mm) loaded in a glass tubular reactor (10 mm internal diameter) and the composition of the outgoing gas stream is measured in real time by means of a previously calibrated Thermal Conductivity Detector (TCD) (Fig. S1). To optimize the detector response, the experiments were performed on a He/CO_2 mixture, as the different thermal conductivity of these gases allows for a very accurate measurement of the quantity of desorbed CO_2. Before the sorbent bed becomes saturated with adsorbed gas, the downstream composition consists only of pure helium due to its negligible affinity for the surface of the structure and high affinity of CO_2 (CO_2 complete adsorption). When the bed is saturated with CO_2, the composition of the outgoing mixture corresponds to that of the incoming mixture (breakthrough). The speed with which the sorbent bed is saturated depends on the amount of sorbent used in the reactor, the total gas flow, the concentration of CO_2 in the mixture and the temperature at which the bed is kept. Following the adsorption, materials were regenerated by TSA inside the instrument furnace applying a 10 °C/min temperature ramp and by MISA at different magnetic fields by means of an induction heating system Ambrell Easyheat 2.4 equipped with a 8-turn coil of 2.5 cm diameter and 4.5 cm high, working at 190 kHz. In this latter case, the furnace is removed from the instrument and the inductor coil is placed around the glass reactor. The coil position can be adjusted to have the sorbent granules placed at its center. The temperature was measured by placing a fiber optic temperature sensor (Opsens Solutions) in the adsorbent bed. The gas flows employed during desorption are usually identical to the adsorption phase flows. Each desorption experiment following the uptake in dynamic conditions has been performed 3–5 times.

The Specific Absortpion Rate (SAR) value was evaluated from the temperature kinetic curve, T(t), by using the following equation:

$$SAR = \frac{\sum_i m_i c_{pi}}{m_{MFC}} \frac{\Delta T}{\Delta t} \quad (1)$$

where m_i is the mass of the i-species involved in the heat exchange and c_{pi} its specific heat, ΔT is the temperature increase in the interval of time Δt and m_{MFC} is the mass of the magnetic composite. Since the measurement is carried out in non-adiabatic conditions, ΔT/Δt value was extrapolated for t→ 0 by considering the initial slope of the temperature kinetic curve. In our case, since the c_p of the MFC (including MNPs, MOF and surfactant) was directly evaluated, the formula reduced to:

$$SAR = c_{pMFC} \frac{\Delta T}{\Delta t} \quad (2)$$

3. Results and discussion

3.1. Structural and morphological characterization

The XRD pattern of the synthesized HKUST-1-magnetite composite (Fig. 1) displays the characteristic reflections of both the organic component (HKUST-1) and magnetite, suggesting that the mechanochemical synthetic approach induces the growth of a well crystallized organic phase. XRD pattern of Fe_3O_4 nanoparticles alone is reported in Supporting Information, Fig. S2.

The thermal stability of the composite was investigated by thermogravimetric analysis (SI Figure S3) and observed weight losses are in accordance with the composition of the material and consistent with HKUST-1 and similar composites [27].

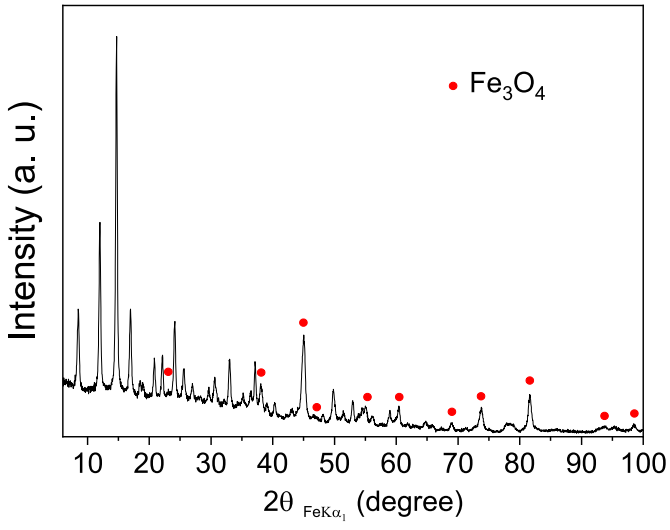

Fig. 1. XRD pattern of the magnetic composite.

The nitrogen adsorption curve at 77 K is reported in Fig. 2 together with the pore size distribution. The composite material shows a combination of type I (at low relative pressure) and type IV (at higher relative pressure) isotherm, typical of samples characterized by the presence of both microporosity and mesoporosity. The nitrogen uptake at low pressure shows the same trend as that measured for HKUST-1. The isotherm in logarithmic scale (inset Fig. 2) highlights a double uptake, confirming the bimodality of the microporosity of HKUST-1 [27], evident also in the pore size distribution curve (Fig. 2b). A relatively broad mesoporosity distribution is also visible in the graph, probably due to the occurrence of some structural disorder of the organic component of the composite and by aggregation phenomena induced by the presence of the nanoparticles. The slope at intermediate pressure regime suggests a non-negligible extension of "non-microporous" surface, in accordance with the presence of hysteresis. The BET area, calculated according to the evaluation criterion developed for microporous materials reported in Ref. [42], is equal to 960 ± 50 m^2/g, remarkably lower than HKUST-1 synthesized in comparable conditions (1800 ± 90 m^2/g). Such decrease is higher than that expected due to the presence of an inorganic, non-adsorbing, phase pointing to a structural disorder in the MOF induced by the presence of nanoparticles. The micropore volume is 0.33 cm^3/g. Compared to the HKUST-1 and in agreement with the other magnetic composites [27] there is a decrease of 52% in the microporous volume value similarly due to the presence of the nanoparticles that change textural properties of the material.

A representative TEM image of TMA coated Fe_3O_4 MNP (Fig. 3, left) shows octahedral nanoparticles with an average diameter of 28 ± 6 nm (d_{TEM}). Moreover, TEM microscopy images (Fig. 3, right) display the formation of a composite with Fe_3O_4 nanoparticles well distributed in the MOF, showing that the incorporation process did not alter the morphological characteristics of the inorganic particles.

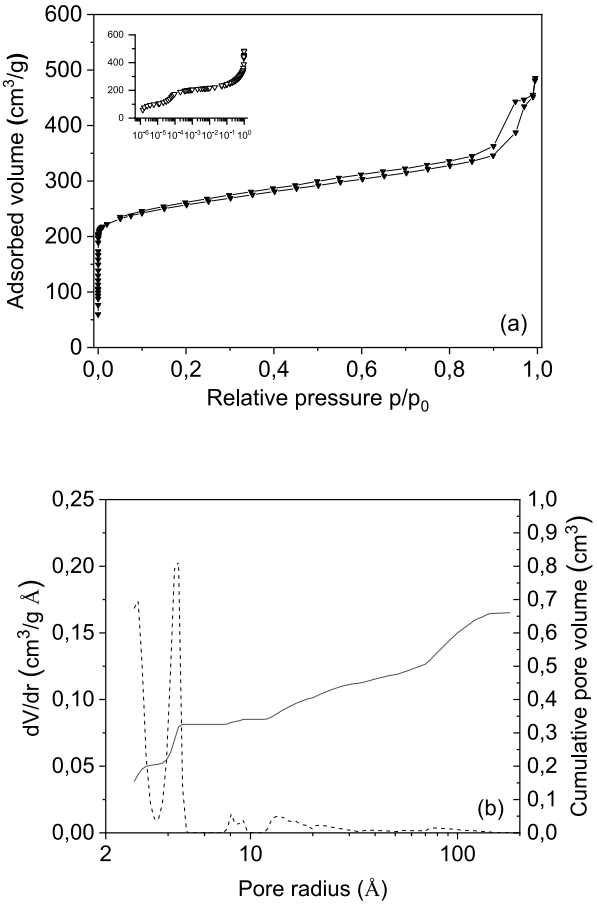

Fig. 2. (a) Adsorption isotherm at 77 K. In the inset the curve is plotted in logarithmic scale to highlight the double uptake at low relative pressure. (b) Pore size distribution (dashed line) and cumulative porous volume.

The XRD diffraction pattern of the sample Fe_3O_4, (Fig. S2 in SI), confirmed the presence of a single crystalline phase with a diffraction pattern compatible with the spinel cubic structure characteristic of magnetite. All the peaks, indeed, match for position and intensity those of the reference pattern (JCPDS 19–0629). The lattice parameter (a = 8.3834(2) Å) is close to the one expected for magnetite (8.396 Å) confirming that the sample consists of magnetite nanoparticles. The crystallite diameter (d_{XRD} = 33.2(4) nm) obtained by the Scherrer analysis is comparable to that obtained by TEM measurement, suggesting that the MNP can be considered as single crystals with a high degree of crystallinity.

3.2. Magnetic characterization

The magnetic properties of the composite were investigated by recording magnetization field dependence at 300 K (Fig. S4, Supporting Information). The sample exhibited magnetic irreversibility with a small coercivity ($\mu_0 H_c \cong$ 4 mT) and reduced remanence ($M_r/M_s \cong$ 0.12), comparable with the values observed for the as-prepared nanoparticles. Similarly, the saturation magnetization (M_s) of the composite, approximated to M@5T, when scaled to the magnetic phase content estimated from ICP analysis (12.9% of Fe_3O_4 in the hydrated sample, 17% on dry basis) was close to that of the pristine nanoparticles (~84 Am^2/kg and ~81 Am^2/kg for HKUST-1-Fe_3O_4 and Fe_3O_4, respectively). This behavior clearly indicates that the incorporation of the MNPs in the metal organic framework did not affect their magnetic properties.

Such values need as well to be compared with analogous Fe_3O_4@HKUST-1 previously synthesized MFC [27]. Those materials, grown on MNP prepared by ball milling, showed Ms in the range 54–70emu/g depending on the synthesis conditions.

One of the functional characterizations essential to define the effectiveness of the developed materials for the application of the MISA technology is the measurement of their ability in dissipating energy when exposed to an alternating magnetic field. The parameter of interest is defined as SAR (Specific Absorption Rate) or SPL (Specific Power Loss) and indicates how much energy per mass unit is absorbed over time by the material in the field conditions in which the measurement is performed (intensity and frequency).

The SAR value of the magnetic composite for an applied AMF of B = 12,6 mT and f = 190 kHz was estimated 1.6 W/g.

4. Carbon dioxide and nitrogen adsorption isotherms

The materials used in adsorption/separation processes must meet several requirements such as high selectivity, high working capacity and low regeneration energies to ensure energy consumption as low as possible [43–46]. Equilibrium adsorption isotherms are typically measured to get this information.

Fig. 4 shows the adsorption isotherms of CO_2 (top panel) and N_2 (bottom panel) measured at different temperatures. The quantity of adsorbed carbon dioxide is high, (i.e., ~5 $mmol/g_{material}$ at 273 K and 1 bar) and, as expected, it decreases as the temperature increases. Conversely, the low affinity of the material for nitrogen is evidenced by considering that at 273 K and 1 bar the adsorbed amount is less than 0.4 mmol/g. Moreover, the material shows a similar adsorption capacity in CO_2 and N_2 compared to the Fe_3O_4-HKUST-1 composites developed in Ref. [27]. The result agrees with the measured specific surface area and with the analysis of the microporosity that does not show significant differences for all the developed composites.

The ideal selectivity values, S, were calculated using the following equation:

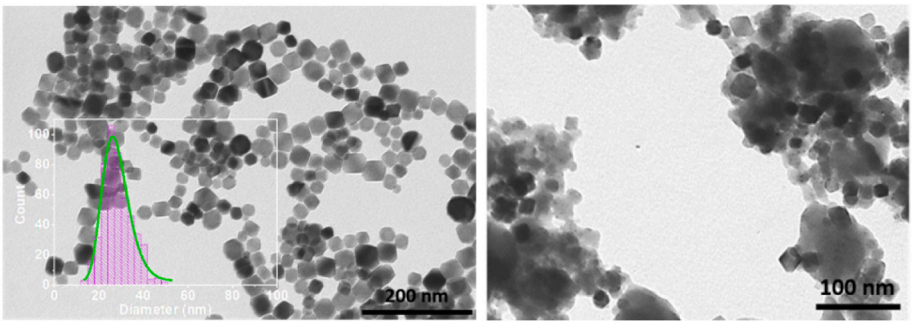

Fig. 3. Representative bright field TEM micrographs of TMA-coated Fe_3O_4 MNPs before (left) and (after) inclusion in HKUST-1. The size distribution of the NPs is shown as inset of the left panel.

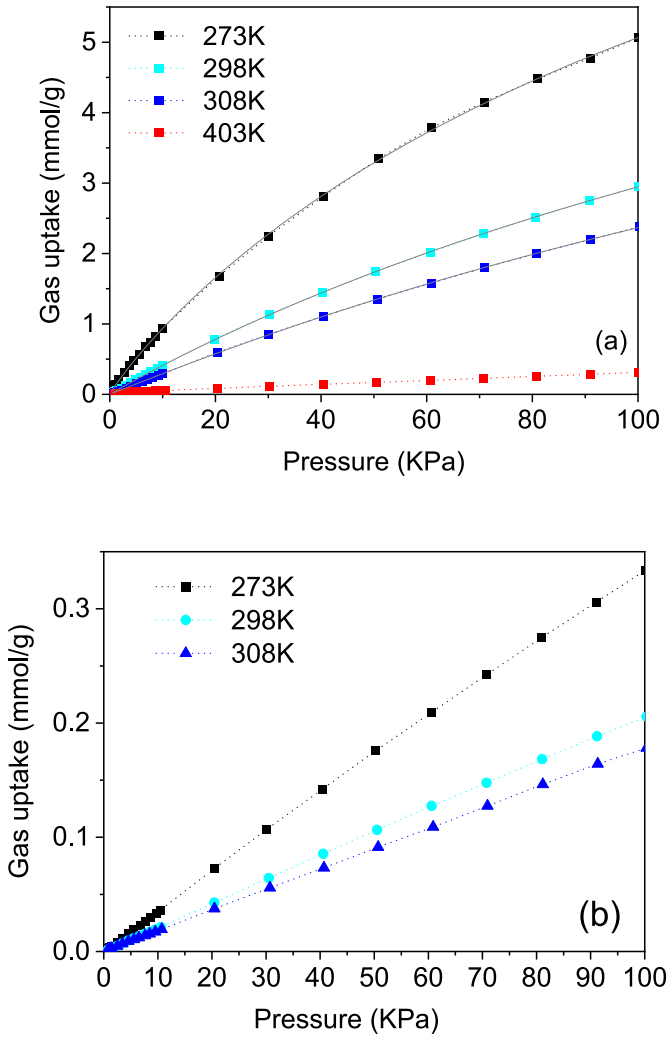

Fig. 4. (a) Experimental adsorption isotherms and Freundlich-Langmuir fit (continuous line) for CO_2 at different temperatures. (b) Experimental nitrogen uptake at different temperatures. Dotted lines are intended as a guide to the eye.

$$S = \frac{q_1/q_2}{p_1/p_2} \tag{3}$$

where q_i represents the quantity of the adsorbed i-component and p_i its partial pressure. For the calculation, the composition 15:75 in CO_2 and N_2 was utilized to mimic that of a post-combustion gas containing 15–16% of CO_2,73–77% of N_2, 4–7% of water vapor and other impurities. The selectivity was found equal to 22, 17 and 14 at 273 K, 298 K and 308 K, respectively, in agreement with values obtained in the previous work [27].

To calculate the working capacity, defined as the difference between the moles of adsorbed CO_2 per mass of adsorbent in the loading conditions (p, T) and the moles of CO_2 desorbed at the selected desorption temperature and pressure 1 bar, a CO_2 isotherm was measured at the desorption temperature 403 K. The calculated working capacity is 0.12 mmol/g utilizing, for the loading conditions, p = 0.15 bar and T = 308 K typical of post-combustion mixture.

The adsorption enthalpy calculated utilizing experimental data from Fig. 4a is 23 kJ/mol (see Supporting Information for the calculation details and Fig. S5 where enthalpy is reported as a function of adsorbed carbon dioxide).

5. Adsorption and desorption dynamics

Breakthrough curves are reported in Fig. 5. Real time carbon dioxide concentration is normalized to the inlet concentration (C/Co). The adsorbed CO_2 amount was obtained by integrating the breakthrough curve according to the equation:

$$Q = \int_{tb}^{tf} \frac{c_0 - c_t}{c_0} f dt \tag{4}$$

where t_b and t_f are the initial and final times after the subtraction of the

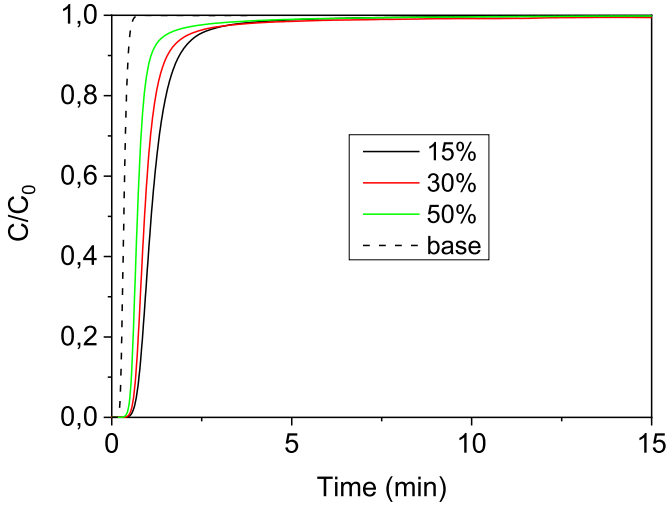

Fig. 5. CO_2 breakthrough curves ($T_{adsorption}$ 32 °C) at different concentrations of carbon dioxide in the mixture. Total flow of He/CO_2 mixture is 50 ml/min. Breakthrough measurements were performed on 0,4 g of material. The figure also shows the output curve of the mixture in the absence of the adsorbent bed (baseline).

baseline, c is the CO_2 concentration in the flow and f is the gas flow.

We observed that, by flowing CO_2 to the reactor at 15% vol, the bed shows a breakthrough time ($C/C_0 = 0.05$) of 0.7 min and is saturated ($C/C_0 = 0.95$) in 2.3 min with linear velocity of the total gas flow of 1.06 cm/s. By increasing the CO_2 concentration, breakthrough times are predictably shorter.

At the end of breakthrough measurement, desorption experiments were performed at different magnetic field amplitudes keeping the incoming flow at 50 ml/min (CO_2 15%vol). Fig. 6 shows the desorption curves (a) and the temperature profiles measured inside the sorbent bed (b) as a function of the application time of the alternating magnetic field. The carbon dioxide desorption starts as soon as the field is applied.

The magnetic field was applied for 10 min, a time judged sufficient to obtain a stable temperature, but the regeneration process is completed in a shorter time. The final temperature measured for the three examples shown are 175 °C, 155 °C and 130 °C, respectively.

Fig. 7 reports the amount of carbon dioxide desorbed (a) and the temperature reached in the sorbent bed (b) as a function of the applied field for the Fe_3O_4@HKUST-1 and, to better highlight the material optimization process, the results are compared to those of the

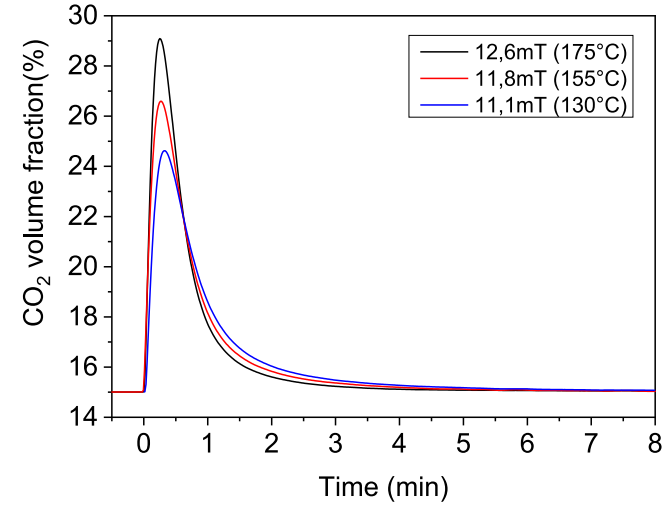

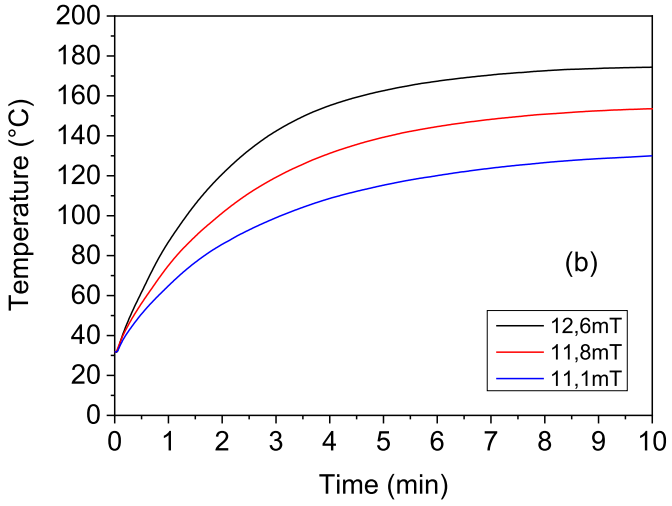

Fig. 6. (a) Carbon dioxide desorption curves at different applied magnetic field. The peaks reveal an increase in the concentration of carbon dioxide in the stream during the application of the magnetic field. In the legend, the maximum temperature reached by the sample under the different experimental conditions is reported in brackets. In (b) the corresponding temperature profiles of the sorbent bed is reported. Total inlet gas flow: 50 ml/min. Sample weight: 0.4 g.

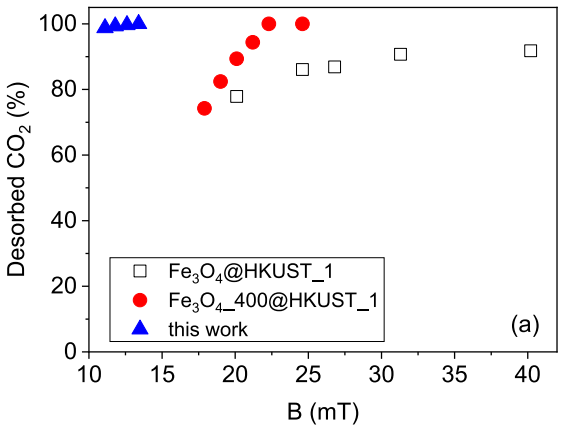

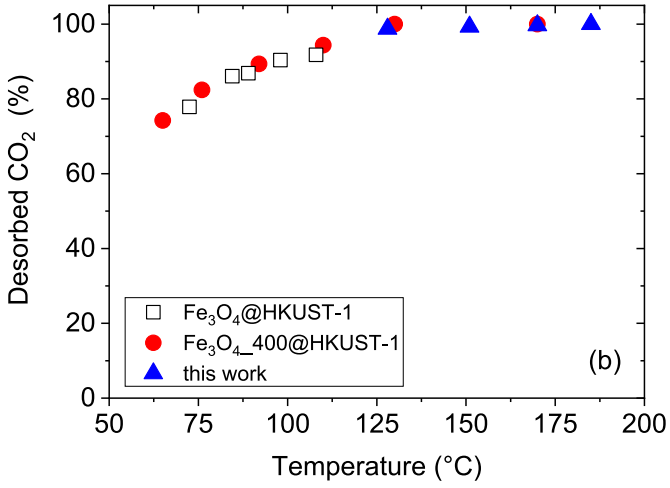

Fig. 7. (a) Relative amount of desorbed carbon dioxide as a function of the applied magnetic field for optimized Fe_3O_4@HKUST-1, Fe_3O_4_400@HKUST-1 and Fe_3O_4@HKUST-1 composites [27]. CO_2 partial pressure is 15%. (b) Desorbed carbon dioxide as a function of the temperature reached in the adsorbent material during MISA. Error bars have the size of the symbols.

composites developed using magnetite MNPs produced via ball milling (Fe_3O_4@HKUST-1 and Fe_3O_4_400@HKUST-1) [27]. As shown in Fig. 7a, the new nanocomposite requires lower magnetic fields to desorb the carbon dioxide accumulated during the breakthrough operation. This is because optimized MNPs have a higher SAR value than those produced by mechanochemical synthesis. By dissipating magnetic energy more efficiently they allow the regeneration temperatures to be reached at much lower fields.

The three composites display similar thermal stability, CO_2 adsorption capacity (see carbon dioxide isotherms) and desorption vs temperature features (Fig. 7b), signifying the robustness of the synthesis method. However, they behave very differently with respect to MISA due to the different intrinsic properties of the MNPs. This result has major implications in calculating the efficiency of the technology as it affects the costs of generating the magnetic field.

6. Evaluation of the efficiency of MISA technology

One of the drawbacks of TSA regeneration process consists in the poor energy transmission efficiency, detectable as high thermal gradients between the reactor wall and the sorbent material, and the associated waste of energy. In addition, most of the sorbent materials show poor thermal conductivity, aggravating the thermal inhomogeneities of the beds and giving rise to the presence of hot-spots, potentially

dangerous for the stability of the materials, and causing long regeneration times.

These limits are overcome by MISA which foreshadows two main advantages: the first is represented by the greater and proven efficiency of magnetic induction compared to other heating methods in the transfer of energy, thus providing energy savings [47]. The second concerns the intensification of the desorption process thanks to the immediate and timely heating of the sorbent bed triggered by the MNPs exposed to the magnetic field. Productivity, (i.e. the frequency with which it is possible to change the temperature of the adsorbent bed) is a parameter to fully evaluate the advantages of MISA technology compared to other heating methods. Heating or cooling the adsorbent bed to reach the pre-established point of adsorption and desorption in the shortest possible time allows for reducing the duration of the entire cycle, thus intensifying the separation procedure.

Desorbed CO_2 concentration profiles, obtained by MISA technology and traditional furnace heating performed on the same sorbent bed, are compared in Fig. 8. Same experimental conditions apply to both MISA and TSA processes. Following the dynamic adsorption in breakthrough experiments, the adsorbent is heated until the temperature of 175 °C is reached and the necessary time is waited for the complete desorption of CO_2. The heating ramp in the furnace was 10 °C/min. Faster heat ramps result in delays in reaching temperature in the sorbent bed due to the insulating nature of MOFs.

Considering the same amount of carbon dioxide adsorbed, regeneration via MISA is completed in 6 min with 90% of the CO_2 recovered already after 1.5 min. The traditional regeneration process, limited by the heat transfer from the source to the material, takes more than 10 min. Since by applying MISA, the stability equilibrium temperature is 175 °C the TSA experiment was performed by heating up to the same temperature. At the temperature of 130 °C, which is the effective temperature to achieve complete desorption, both samples have already desorbed 95% of CO_2 in 2.5 min and 9.6 min, respectively.

In consideration of the very different desorption rates, MISA is more competitive than regular TSA (see also Fig. S6, Supporting Information) allowing for an increased number of adsorption/desorption cycles and hence higher productivity. Furthermore, it should be noted that there is a mass effect in the heating rate of the adsorbent bed due to the minimization of thermal dispersion as the productivity measured for the same material increases with the mass. Therefore, further margins of improvement can be figured out.

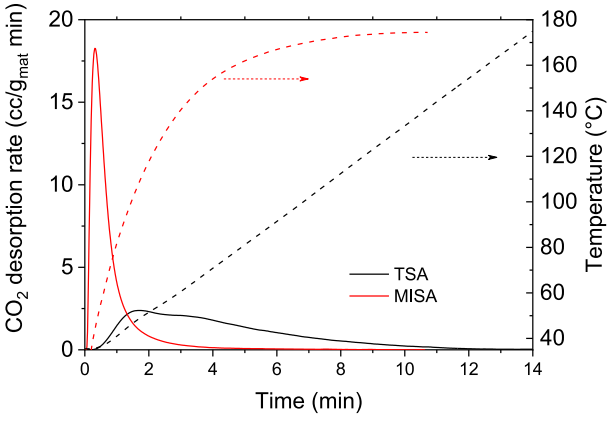

Fig. 8. Regeneration of the optimized Fe_3O_4@HKUST-1 sorbent bed (0.4 g) by MISA (B = 12.6 mT) and by traditional furnace heating from outside, TSA (heating rate 10 °C/min). Dashed line correspond to the temperature recorded during the two experiments.

6.1. Determination of the regeneration energy

The regeneration energy ***Q*** allows the estimation of the thermal energy requirement per unit mass of CO_2 captured in a typical CCS process. This is the sum of the energy required to heat the adsorbent to the desorption temperature and the energy required for the desorption process. It can be expressed by the following equation:

$$\boldsymbol{Q} = \frac{\boldsymbol{c_p m_{sorb} \Delta T + \Delta H_{CO2} \Delta q_{CO2}}}{\boldsymbol{m_{CO2}}} \quad (5)$$

where c_p is the specific heat capacity of the adsorbent (J/gK), m_{sorb} is the mass of the adsorbent (g), ΔT is the temperature difference between adsorption and desorption (K), ΔH_{CO2} is the heat of desorption of CO_2 (kJ/mol) for the sorbent material, Δq is the working capacity, and m_{CO2} is the mass of CO_2 captured.

For the composite here developed, the c_p value was measured in the temperature range 35–130 °C and found to vary between 0.91 and 1.07 $J/g_{MFC}K$. The most unfavorable figure, 1.07, was used in the calculations. The working capacity was determined from the adsorption isotherms at 308 K and 403 K reported in Fig. 4. The calculated regeneration energy and all the useful data are reported in Table 1. In addition, the thermal work performed by the magnetic material (amount of energy dissipated by the MNPs) is also reported, calculated by multiplying the SAR (W/g) by the weight of the sample and the field application time. The ratio of regeneration energy to thermal work gives the thermal efficiency of induction heating.

For Fe_3O_4-HKUST-1 the regeneration energy is 4.4 $MJ/kgCO_2$, a value in line with data reported in other works [19,23] but higher than that estimated for MEA (aqueous monoethanolamine solution) processes (ca 3 MJ/kg) commonly in use. The low working capacity of the sorbent is the factor that most negatively affects the regeneration energy in this work. Therefore, in order for this type of composite material to establish itself in the panorama of separation technologies, the use of more performing MOFs [43–46,48,49] is recommended. Furthermore, HKUST-1, despite its good adsorption capacity and selectivity, is unstable in streams containing water vapor and an energy penalty should be added for water condensation.

The thermal energies were also calculated for a regeneration of the material equal to 95%, considering that to recover the remaining 5% of CO_2, the desorption time doubles with the consequent consumption of energy to generate the magnetic field. The calculation of quantities not defined in the text is reported in the supporting info.

The obtained values of thermal efficiency can be improved by developing composites with better CO_2 adsorption capacity and shorter regeneration times.

Table 1
Data used for the calculation of the regeneration energy and the heating thermal efficiency. The definition and calculation of some quantities is reported in SI.

Magnetic field amplitude (mT)	12.6
Frequency (kHz)	190
m_{sorb} (g)	0.4
SAR_{MFC} (W/g)	1.6
ΔH_{ads}(kJ/mol)	23
Working capacity (mmol/g)	0.12
Regeneration time (100%) (s)	270
Regeneration time (95%) (s)	135
Desorbed mCO_2(g)	0.00982
Thermal work required (J)	42.8
Thermal Energy dissipated by MFC (100%) (J)	173
Thermal Energy dissipated by MFC (95%) (J)	86
Desorption Temperature (°C)	130
Regeneration Energy Q (MJ/kg)CO_2	4.4
Thermal efficiency (100%) (%)	25,4
Thermal efficiency (95%) (%)	50,8

7. Conclusions

An optimized Fe_3O_4@HKUST-1 nanocomposite for the Magnet Induction Swing Adsorption was developed and fully characterized. The new material consists of ~28 nm Fe_3O_4 nanoparticles with high crystallinity and improved magnetic property well embedded in the MOF matrix. Moreover, the mechanochemical method used to synthetize the composite does not alter both the physico-chemical properties and morpho structural features of the MNPs and the material crystallinity of the MOF HKUST-1 is largely preserved. The CO_2 adsorption capacity is comparable to that observed for the composites prepared in our previous work using magnetite NP synthesized by ball milling, indicating that for the same amount of incorporated magnetic material, there is no appreciable influence of nanoparticles on the sorbent capacity of the composite. However, due to the higher SAR value, the optimized nanocomposite requires lower magnetic fields to desorb the CO_2 and allows for reaching the same regeneration temperature in the sorbent bed at lower magnetic field amplitude.

Regardless of the insulating properties of the MOF, the high CO_2 release rate was due to the induction heating system's localized heating. The MISA process's efficiency proved to be highly reliant on the material's magnetic properties. Induction heating as an alternative electrified heating method for carbon capture processes has proven to be a viable option.

The productivity of the adsorption/desorption cycle is linked to the duration of the two stages. While in the low temperature adsorption stage the speed of diffusion of the gas inside the sorbent material (mass transfer) dominates, in the desorption stage the heat transfer rate is fundamental to reach the temperature set point in the shortest possible time. Since the productivity of the entire procedure, which is of fundamental importance for real applications, depends on the frequency of the adsorption/desorption cycle, the shorter the regeneration time, the greater the productivity of the system, which can be translated into greater production capacity.

CRediT authorship contribution statement

Mariangela Bellusci: Conceptualization, Formal analysis, writing, Supervision. **Martin Albino:** Investigation, Formal analysis, writing. **Andrea Masi:** Investigation, Formal analysis. **Davide Peddis:** Investigation, Formal analysis, writing. **Claudia Innocenti:** Investigation, Formal analysis. **Francesca Varsano:** Conceptualization, Formal analysis, writing.

Declaration of competing interest

The authors declare that they have no known competing financial interests or personal relationships that could have appeared to influence the work reported in this paper.

Data availability

Data will be made available on request.

Acknowledgements

This work was supported by MISE within the framework of the Accordo di Programma Ministero dello Sviluppo Economico-ENEA, PTR2019–2021 Project 1.6 "Efficienza energetica dei prodotti e dei processi industriali".

Appendix A. Supplementary data

Supplementary data to this article can be found online at https://doi.org/10.1016/j.matchemphys.2023.128525.

References

[1] M. Ambrosetti, A perspective on power-to-heat in catalytic processes for decarbonization, Chem. Eng. Proces. - Proces. Intensificat. 182 (2022), 109187, https://doi.org/10.1016/j.cep.2022.109187.
[2] C. Scarfiello, M. Bellusci, L. Pilloni, D. Pietrogiacomi, A. La Barbera, F. Varsano, Supported catalysts for induction-heated steam reforming of methane, Int. J. Hydrogen Energy 46 (2021) 134–145, https://doi.org/10.1016/j.ijhydene.2020.09.262.
[3] F. Varsano, M. Bellusci, A. La Barbera, M. Petrecca, M. Albino, C. Sangregorio, Dry reforming of methane powered by magnetic induction, Int. J. Hydrogen Energy 44 (2019), https://doi.org/10.1016/j.ijhydene.2019.02.055.
[4] M.G. Vinum, M.R. Almind, J.S. Engbæk, S.B. Vendelbo, M.F. Hansen, C. Frandsen, J. Bendix, P.M. Mortensen, Dual-function cobalt–nickel nanoparticles tailored for high-temperature induction-heated steam methane reforming, Angew. Chem. Int. Ed. 57 (2018) 10569–10573, https://doi.org/10.1002/anie.201804832.
[5] M.R. Almind, M.G. Vinum, S.T. Wismann, M.F. Hansen, S.B. Vendelbo, J. S. Engbæk, P.M. Mortensen, I. Chorkendorff, C. Frandsen, Optimized CoNi nanoparticle composition for curie-temperature-controlled induction-heated catalysis, ACS Appl. Nano Mater. 4 (2021) 11537–11544, https://doi.org/10.1021/acsanm.1c01941.
[6] J. Marbaix, N. Mille, L.-M. Lacroix, J.M. Asensio, P.-F. Fazzini, K. Soulantica, J. Carrey, B. Chaudret, Tuning the composition of FeCo nanoparticle heating agents for magnetically induced catalysis, ACS Appl. Nano Mater. 3 (2020) 3767–3778, https://doi.org/10.1021/acsanm.0c00444.
[7] A. Bordet, L.M. Lacroix, P.F. Fazzini, J. Carrey, K. Soulantica, B. Chaudret, Magnetically induced continuous CO2Hydrogenation using composite iron carbide nanoparticles of exceptionally high heating power, Angew. Chem. Int. Ed. 55 (2016) 15894–15898, https://doi.org/10.1002/anie.201609477.
[8] S. Hamzehlouia, S.A. Jaffer, J. Chaouki, Microwave heating-assisted catalytic dry reforming of methane to syngas, Sci. Rep. 8 (2018) 8940, https://doi.org/10.1038/s41598-018-27381-6.
[9] H.M. Nguyen, G.H. Pham, R. Ran, R. Vagnoni, V. Pareek, S. Liu, Dry reforming of methane over Co–Mo/Al 2 O 3 catalyst under low microwave power irradiation, Catal. Sci. Technol. 8 (2018) 5315–5324, https://doi.org/10.1039/C8CY01601A.
[10] E. Meloni, M. Martino, A. Ricca, V. Palma, Ultracompact methane steam reforming reactor based on microwaves susceptible structured catalysts for distributed hydrogen production, Int. J. Hydrogen Energy 46 (2021) 13729–13747, https://doi.org/10.1016/j.ijhydene.2020.06.299.
[11] A. Bogaerts, X. Tu, J.C. Whitehead, G. Centi, L. Lefferts, O. Guaitella, F. Azzolina-Jury, H.-H. Kim, A.B. Murphy, W.F. Schneider, T. Nozaki, J.C. Hicks, A. Rousseau, F. Thevenet, A. Khacef, M. Carreon, The 2020 plasma catalysis roadmap, J. Phys. D Appl. Phys. 53 (2020), 443001, https://doi.org/10.1088/1361-6463/ab9048.
[12] M. Ambrosetti, A. Beretta, G. Groppi, E. Tronconi, A numerical investigation of electrically-heated methane steam reforming over structured catalysts, Frontiers Chem. Eng. 3 (2021) 1–17, https://doi.org/10.3389/fceng.2021.747636.
[13] L. Zheng, M. Ambrosetti, D. Marangoni, A. Beretta, G. Groppi, E. Tronconi, Electrified methane steam reforming on a washcoated <scp>SiSiC</scp> foam for low-carbon hydrogen production, AIChE J. (2022), https://doi.org/10.1002/aic.17620.
[14] S.T. Wismann, J.S. Engbæk, S.B. Vendelbo, F.B. Bendixen, W.L. Eriksen, K. Aasberg-Petersen, C. Frandsen, I. Chorkendorff, P.M. Mortensen, Electrified methane reforming: a compact approach to greener industrial hydrogen production, Science 364 (2019) 756–759, https://doi.org/10.1126/science.aaw8775, 1979.
[15] M.M. Sadiq, H. Li, A.J. Hill, P. Falcaro, M.R. Hill, K. Suzuki, Magnetic induction swing adsorption: an energy efficient route to porous adsorbent regeneration, Chem. Mater. 28 (2016) 6219–6226, https://doi.org/10.1021/acs.chemmater.6b02409.
[16] H. Li, M.M. Sadiq, K. Suzuki, R. Ricco, C. Doblin, A.J. Hill, S. Lim, P. Falcaro, M. R. Hill, Magnetic metal-organic frameworks for efficient carbon dioxide capture and remote trigger release, Adv. Mater. 28 (2016) 1839–1844, https://doi.org/10.1002/adma.201505320.
[17] M.M. Sadiq, M. Rubio-Martinez, F. Zadehahmadi, K. Suzuki, M.R. Hill, Magnetic framework composites for low concentration methane capture, Ind. Eng. Chem. Res. 57 (2018) 6040–6047, https://doi.org/10.1021/acs.iecr.8b00810.
[18] M.M. Sadiq, K. Konstas, P. Falcaro, A.J. Hill, K. Suzuki, M.R. Hill, Engineered porous nanocomposites that deliver remarkably low carbon capture energy costs, Cell Rep Phys Sci 1 (2020), 100070, https://doi.org/10.1016/j.xcrp.2020.100070.
[19] M.R. Rahimi, S. Mosleh, Magnetic and electrical-assisted adsorption processes, in: Intensification of Sorption Processes, Elsevier, 2022, pp. 71–93, https://doi.org/10.1016/B978-0-12-821411-4.00005-5.
[20] K. Baamran, K. Newport, A.A. Rownaghi, F. Rezaei, Development and assessment of magnetic Fe2O3@MOF-74 composite sorbents for ethylene/ethane separation, Chem. Eng. J. 451 (2023), https://doi.org/10.1016/j.cej.2022.139006.
[21] M.M. Sadiq, K. Suzuki, M.R. Hill, Towards energy efficient separations with metal organic frameworks, Chem. Commun. 54 (2018) 2825–2837, https://doi.org/10.1039/C8CC00331A.
[22] B. He, M.M. Sadiq, M.P. Batten, K. Suzuki, M. Rubio-Martinez, J. Gardiner, M. R. Hill, Continuous flow synthesis of a Zr magnetic framework composite for post-combustion CO $_2$ capture, Chem. Eur J. 25 (2019) 13184–13188, https://doi.org/10.1002/chem.201902560.
[23] M. Gholami, B. Verougstraete, R. Vanoudenhoven, G.V. Baron, T. Van Assche, J.F. M. Denayer, Induction heating as an alternative electrified heating method for carbon capture process, Chem. Eng. J. 431 (2022), https://doi.org/10.1016/j.cej.2021.133380.

[24] X. Lin, B. Shao, J. Zhu, F. Pan, J. Hu, M. Wang, H. Liu, In situ electromagnetic induction heating for CO2Temperature swing adsorption on magnetic Fe3O4/N-doped porous carbon, Energy Fuel. 34 (2020) 14439–14446, https://doi.org/10.1021/acs.energyfuels.0c02699.
[25] I. Morales, M. Muñoz, C.S. Costa, J.M. Alonso, J.M. Silva, M. Multigner, M. Quijorna, M.R. Ribeiro, P. de la Presa, Induction heating in nanoparticle impregnated zeolite, Materials 13 (2020), https://doi.org/10.3390/ma13184013.
[26] K. Newport, K. Baamran, A.A. Rownaghi, F. Rezaei, Magnetic-field assisted gas desorption from Fe2O3/zeolite 13X sorbent monoliths for biogas upgrading, Ind. Eng. Chem. Res. 61 (2022) 18843–18853, https://doi.org/10.1021/acs.iecr.2c02969.
[27] M. Bellusci, A. Masi, M. Albino, D. Peddis, M. Petrecca, C. Sangregorio, A. La Barbera, F. Varsano, Fe3O4@HKUST-1 magnetic composites by mechanochemical route for induction triggered release of carbon dioxide, Microporous Mesoporous Mater. 328 (2021), https://doi.org/10.1016/j.micromeso.2021.111458.
[28] Z. Wang, S.M. Cohen, Postsynthetic modification of metal–organic frameworks, Chem. Soc. Rev. 38 (2009) 1315, https://doi.org/10.1039/b802258p.
[29] J.-L. Do, T. Friščić, Mechanochemistry: a force of synthesis, ACS Cent. Sci. 3 (2017) 13–19, https://doi.org/10.1021/acscentsci.6b00277.
[30] J.L. Dormann, D. Fiorani, E. Tronc, Magnetic Relaxation Fine-Particle Sys. (1997) 283–494, https://doi.org/10.1002/9780470141571.ch4.
[31] D. Fiorani, D. Peddis, Understanding dynamics of interacting magnetic nanoparticles: from the weak interaction regime to the collective superspin glass state, J. Phys. Conf. Ser. 521 (2014), 012006, https://doi.org/10.1088/1742-6596/521/1/012006.
[32] O.L. Lanier, O.I. Korotych, A.G. Monsalve, D. Wable, S. Savliwala, N.W.F. Grooms, C. Nacea, O.R. Tuitt, J. Dobson, Evaluation of magnetic nanoparticles for magnetic fluid hyperthermia, Int. J. Hyperther. 36 (2019) 686–700, https://doi.org/10.1080/02656736.2019.1628313.
[33] A.A. de Almeida, E. De Biasi, M.V. Mansilla, D.P. Valdés, H.E. Troiani, G. Urretavizcaya, T.E. Torres, L.M. Rodríguez, D.E. Fregenal, G.C. Bernardi, E. L. Winkler, G.F. Goya, R.D. Zysler, E. Lima, Magnetic hyperthermia experiments with magnetic nanoparticles in clarified butter oil and paraffin: a thermodynamic analysis, J. Phys. Chem. C 124 (2020) 27709–27721, https://doi.org/10.1021/acs.jpcc.0c06843.
[34] Y. Du, X. Liu, Q. Liang, X.-J. Liang, J. Tian, Optimization and Design of magnetic ferrite nanoparticles with uniform tumor distribution for highly sensitive MRI/MPI performance and improved magnetic hyperthermia therapy, Nano Lett. 19 (2019) 3618–3626, https://doi.org/10.1021/acs.nanolett.9b00630.
[35] M.H.A. Guedes, N. Sadeghiani, D.L.G. Peixoto, J.P. Coelho, L.S. Barbosa, R. B. Azevedo, S. Kückelhaus, M. de F. Da Silva, P.C. Morais, Z.G.M. Lacava, Effects of AC magnetic field and carboxymethyldextran-coated magnetite nanoparticles on mice peritoneal cells, J. Magn. Magn Mater. 293 (2005) 283–286, https://doi.org/10.1016/j.jmmm.2005.02.052.
[36] L.C. Branquinho, M.S. Carrião, A.S. Costa, N. Zufelato, M.H. Sousa, R. Miotto, R. Ivkov, A.F. Bakuzis, Effect of magnetic dipolar interactions on nanoparticle heating efficiency: implications for cancer hyperthermia, Sci. Rep. 3 (2013) 2887, https://doi.org/10.1038/srep02887.
[37] A. Urtizberea, E. Natividad, A. Arizaga, M. Castro, A. Mediano, Specific absorption rates and magnetic properties of ferrofluids with interaction effects at low concentrations, J. Phys. Chem. C 114 (2010) 4916–4922, https://doi.org/10.1021/jp912076f.
[38] C. Martinez-Boubeta, K. Simeonidis, D. Serantes, I. Conde-Leborán, I. Kazakis, G. Stefanou, L. Peña, R. Galceran, L. Balcells, C. Monty, D. Baldomir, M. Mitrakas, M. Angelakeris, Adjustable hyperthermia response of self-assembled ferromagnetic Fe-MgO core-shell nanoparticles by tuning dipole-dipole interactions, Adv. Funct. Mater. 22 (2012) 3737–3744, https://doi.org/10.1002/adfm.201200307.
[39] J. Park, E. Lee, N.-M. Hwang, M. Kang, S.C. Kim, Y. Hwang, J.-G. Park, H.-J. Noh, J.-Y. Kim, J.-H. Park, T. Hyeon, One-nanometer-scale size-controlled synthesis of monodisperse magnetic iron oxide nanoparticles, Angew. Chem. Int. Ed. 44 (2005) 2872–2877, https://doi.org/10.1002/anie.200461665.
[40] T. Hyeon, Chemical synthesis of magnetic nanoparticles, Chem. Commun. (2003) 927–934, https://doi.org/10.1039/b207789b.
[41] N.A. Seaton, J.P.R.B. Walton, N. quirke, A new analysis method for the determination of the pore size distribution of porous carbons from nitrogen adsorption measurements, Carbon N Y 27 (1989) 853–861, https://doi.org/10.1016/0008-6223(89)90035-3.
[42] Y.-S. Bae, A.Ö. Yazaydın, R.Q. Snurr, Evaluation of the BET method for determining surface areas of MOFs and zeolites that contain ultra-micropores, Langmuir 26 (2010) 5475–5483, https://doi.org/10.1021/la100449z.
[43] K. Adil, P.M. Bhatt, Y. Belmabkhout, S.M.T. Abtab, H. Jiang, A.H. Assen, A. Mallick, A. Cadiau, J. Aqil, M. Eddaoudi, Valuing metal–organic frameworks for postcombustion carbon capture: a benchmark study for evaluating physical adsorbents, Adv. Mater. 29 (2017) 1–10, https://doi.org/10.1002/adma.201702953.
[44] P. Nugent, E.G. Giannopoulou, S.D. Burd, O. Elemento, E.G. Giannopoulou, K. Forrest, T. Pham, S. Ma, B. Space, L. Wojtas, M. Eddaoudi, M.J. Zaworotko, Porous materials with optimal adsorption thermodynamics and kinetics for co2 separation, Nature 495 (2013) 80–84, https://doi.org/10.1038/nature11893.
[45] Z. Hu, Y. Wang, B.B. Shah, D. Zhao, CO 2 capture in metal-organic framework adsorbents: an engineering perspective, Adv. Sustain. Syst. 3 (2019), 1800080, https://doi.org/10.1002/adsu.201800080.
[46] R.L. Siegelman, E.J. Kim, J.R. Long, Porous materials for carbon dioxide separations, Nat. Mater. 20 (2021) 1060–1072, https://doi.org/10.1038/s41563-021-01054-8.
[47] A. Kirschning, L. Kupracz, J. Hartwig, New synthetic opportunities in miniaturized flow reactors with inductive heating, Chem. Lett. 41 (2012) 562–570, https://doi.org/10.1246/cl.2012.562.
[48] R. Aniruddha, I. Sreedhar, B.M. Reddy, MOFs in carbon capture-past, present and future, J. CO2 Util. 42 (2020), 101297, https://doi.org/10.1016/j.jcou.2020.101297.
[49] N. Kundu, S. Sarkar, Porous organic frameworks for carbon dioxide capture and storage, J. Environ. Chem. Eng. 9 (2021), 105090, https://doi.org/10.1016/j.jece.2021.105090.